Available online at www.sciencedirect.com
SCIENCE DIRECT®
Journal of Molecular Structure 695–696 (2004) 269–286
Journal of MOLECULAR STRUCTURE
www.elsevier.com/locate/molstruc

Temperature dependence of self- and N_2-broadening and pressure-induced shifts in the $3 \leftarrow 0$ band of CO

A. Predoi-Cross[a,c,*], C. Hnatovsky[b,c], K. Strong[c], J.R. Drummond[c], D. Chris Benner[d]

[a]*Department of Physics, The University of Lethbridge, 4401 University Drive, Lethbridge, Alta., Canada T1K 3M4*
[b]*National Research Council, Institute of Microstructural Sciences, and Physics Department, University of Ottawa, 150 Louis Pasteur, Ottawa, Ont., Canada*
[c]*Department of Physics, University of Toronto, Toronto, Ont., Canada M5S 1A7*
[d]*Department of Physics, The College of William and Mary, Box 8795, Williamsburg, VA 23187-8795, USA*

Received 31 October 2003; accepted 11 December 2003

Abstract

A variable-temperature single-pass absorption gas cell with an optical pathlength of 147.5 cm was designed and built for spectroscopic measurements of gases of atmospheric interest. The cell is optically matched to a Bomem DA8.3 Fourier transform spectrometer. A heating/cooling system enveloping the cell, used together with a Neslab ULT-80 thermal bath, allows spectroscopic studies of gas samples at temperatures ranging from 205 to 350 K and at pressures up to 1 atm. Tests of the optical, thermal, and vacuum operation of the system were performed. Spectra of the $3 \leftarrow 0$ vibrational–rotational band of carbon monoxide were recorded from 225 to 348 K and used to determine the rotational gas temperatures. These results were compared with values obtained using thermocouples, in order to assess the thermal performance of the new system. A second temperature-controlled cell 25-cm long, able to withstand pressures up to 30 atm, was also used to record CO spectra. We have recorded high-resolution FTIR spectra of CO and CO perturbed by N_2 at temperatures from 295 to 348 K. The spectra were analyzed to determine pressure broadening and pressure-induced shift coefficients, along with their temperature dependence for several transitions in the second overtone band of CO. The results, especially for self-broadening, are in excellent agreement with other recent measurements reported in the literature.

1. Introduction

Over the past two decades, ground-based and satellite remote sounding spectroscopic techniques have been employed to monitor the concentrations of gases of atmospheric interest. Ultimately, the accuracy of the analysis of the data recorded by all these sounding techniques depend entirely upon having available accurate spectroscopic data for the gases of interest as a function of temperature and pressure. While significant advances have been made in the determination of CO line parameters in the second overtone band [1–9], including broadening and shift coefficients, the temperature dependences of the broadening and shift coefficients have not been studied extensively.

In the first part of this study, we present a new experimental facility designed in our laboratory for the measurement of spectroscopic features and the study of their temperature dependence in the infrared, visible and ultraviolet spectral regions. This new facility meets these requirements by combining the high resolution of the Fourier transform spectrometer along with the high thermal and pressure stability of the gas samples under investigation and elimination of spectral contamination caused by external gases such as H_2O and CO_2. A 25-cm long heatable cell was used to record additional CO spectra. In the second part of this study, we report measurements of high-resolution absorption spectra of CO self-broadened and broadened by nitrogen at temperatures in the 225–348 K range. The spectra were analyzed to determine pressure-broadened line-widths and shifts over the range of temperatures for many transitions in the second overtone band of CO. These values have

* Corresponding author. Tel.: +1-403-329-2697; fax: +1-403-329-2057.
E-mail address: adriana.predoicross@uleth.ca (A. Predoi-Cross).

0022-2860/$ - see front matter © 2004 Elsevier B.V. All rights reserved.
doi:10.1016/j.molstruc.2003.12.043

been used to determine the temperature dependence of the self- and N_2-broadening and shift coefficients for the CO lines.

2. The new experimental facility

2.1. The Fourier transform spectrometer

The Bomem DA8.3 Fourier transform spectrometer utilizes a Twyman–Green interferometer that has a best resolution of 0.0026 cm^{-1} at 4000 cm^{-1}. The output of the spectrometer is a $f/4$ sample beam produced by a 90° off-axis parabolic mirror with an effective focal length of 32.4 cm. The operational vacuum inside the spectrometer is 0.3 Torr using a two-stage rotary pump with pumping speed of 1.5 l/s. The general layout of the system is shown in Fig. 1.

2.2. The transfer optics

The transfer optics used in the facility are responsible for the localization of the interference pattern produced by the interferometer at the detector. The configuration for the transfer optics is illustrated in Fig. 2.

The 90° off-axis parabolic mirror of the Bomem DA8.3 Fourier transform spectrometer forms a convergent $f/4$-beam which is relayed through the 147.5-cm long gas cell and focused on the detector. In order to collimate and re-direct this beam along the axis of the inner cell (Fig. 1), a 90° off-axis (Aero Research Company) parabolic mirror PM_1 with an effective focal length of 20.4 cm and a diameter of 5.1 cm is used. The entrance optics are enclosed in an evacuated tank (Transfer Optics Tank I, in Fig. 1). After mirror PM_1, the collimated beam traverses the entrance window W_1 of the inner cell and the gas sample and leaves the inner cell through the exit window W_2.

The beam after reflection by PM_1 has some divergence caused by the finite size of the light source. For PM_1, the source is represented by the image of the entrance iris diaphragm of the Twyman–Green interferometer inside the Bomem DA8.3 spectrometer. The angle of divergence, θ, can be determined from the relationship $\theta = r/f$, where f is the effective focal length of PM_1, and r is the radius of the iris image. The radius of the entrance iris can be varied from 0.5 to 10 mm and its image at D_1 has the same diameter because the collimating and the focusing mirrors inside the interferometer have equal effective focal lengths. The distance between the center of PM_1 and the plane of W_2 is about 200 cm.

Another 90° off-axis parabolic mirror, PM_2, with an effective focal length of 32.4 cm and diameter of 9.6 cm (ABB Bomem Inc.) focuses and re-directs the beam along the axis of the second evacuable transfer optics tank. After the focal point of PM_2, at D_2, the divergent beam is collected by the elliptical mirror EM and is focused on the detector. Both parabolic mirrors PM_1 and PM_2 are made of solid aluminum coated with a protective layer of magnesium fluoride (MgF_2) to prevent oxidation and ensure high reflectance from the ultraviolet to the infrared region. The iris diaphragms D_1 and D_2 filter out the diffracted light produced by the ruled surfaces of the diamond-turned mirrors inside the spectrometer and the cell. The use of evacuated transfer optics tanks eliminates spurious absorption by gases outside of the actual absorption cell.

Both mirrors PM_1 and PM_2 are mounted inside the facility by means of adjustable opto-mechanical supports, which differ only in their size. These mounts were designed

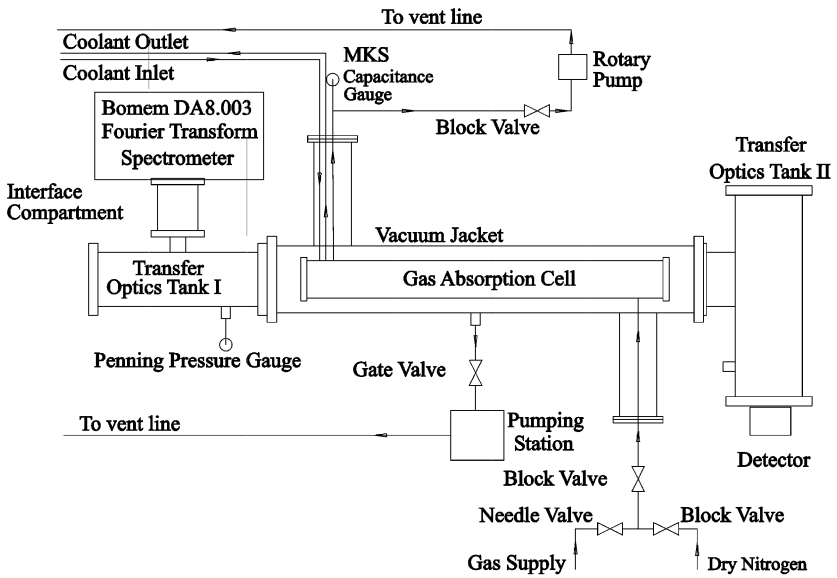

Fig. 1. General layout of the experimental set-up.

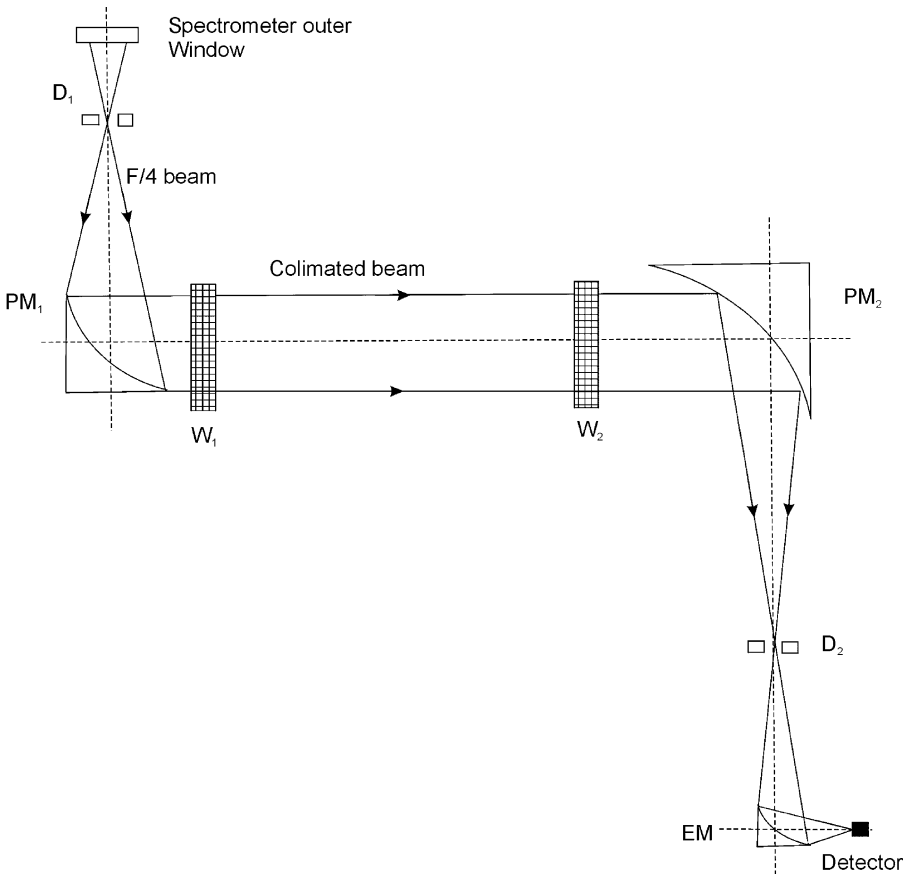

Fig. 2. The design of the transfer optics.

to provide three-dimensional control of the mirror position (three degrees of translational motion and three degrees of angular motion). Coarse rotation and translational motion along the *z*-axis are achieved by moving and rotating the whole assembly with respect to the mechanical axis of the cylindrical transfer optics tank. Fine rotation adjustments are produced by applying differential torques to screws attached to the mounts.

2.3. The gas cell and thermal control system

As shown in Fig. 3, the absorption cell is surrounded by a cooling/heating system and a vacuum jacket. The optical length of the gas absorption cell is 147.5 cm; the optical ports welded to the gas cell have a diameter of 8 cm and are provided with independent electrical heaters to remove thermal gradients along the gas cell. All mechanical and vacuum components for the gas cell are made of stainless steel.

The windows used in the facility are made of UV-grade synthetic fused silica. To suppress channel spectra caused by multiple reflections of the sample beam between the surfaces of the windows, the windows were wedged at an angle of 30 arcmin. The inside surfaces of the windows were positioned at about 1° with respect to each other. This small

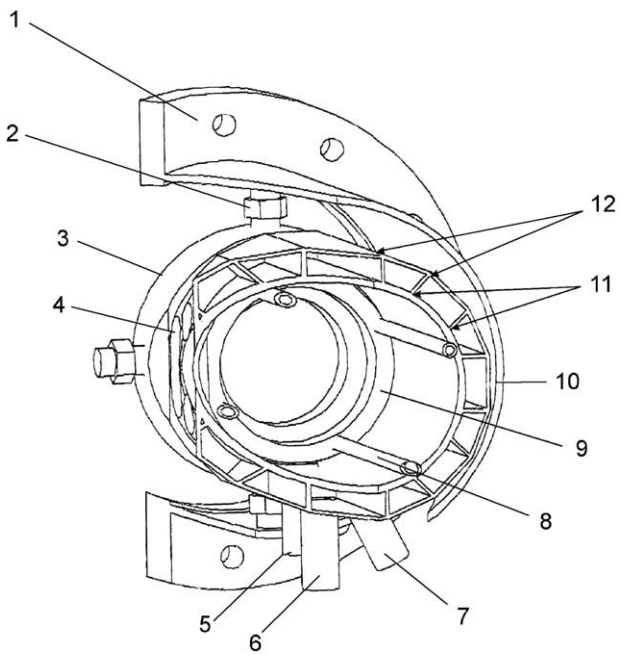

Fig. 3. A cross-sectional view of the gas absorption cell and the vacuum jacket. 1, vacuum jacket; 2, adjustment post; 3, gas absorption cell; 4, electrical heaters; 5, gas inlet; 6, heat carrier inlet; 7, heat carrier outlet; 8, thermocouple channels; 9, yoke-like mount for the thermocouple channels; 10, heat carrier channels; 11, welds for U-shaped channels; 12, welds for strips.

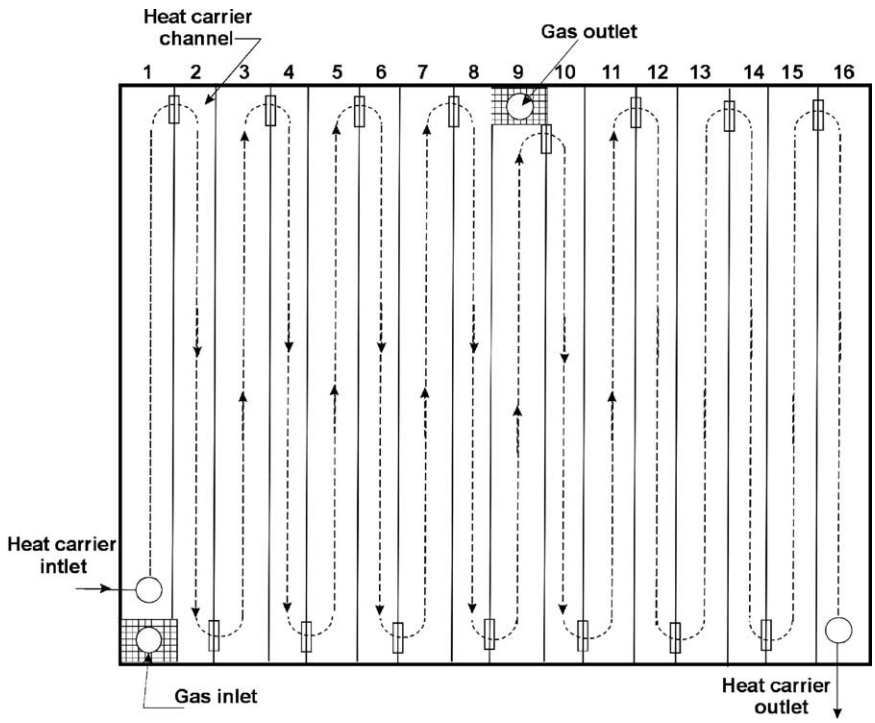

Fig. 4. Schematic diagram of the heating/cooling system.

angle was adjusted using an external He–Ne laser. The windows have a diameter of 10 cm and thickness of 0.8 cm at the thicker edge. For fused silica, with an apparent elastic limit of 6.8×10^7 N/m^2 [10], and an unsupported window diameter of 8 cm, windows of this thickness can withstand pressure gradients up to 8 atm with a safety factor of 4, which determines the maximum pressure of the gas samples [10].

It is not a trivial matter to make a large absorption cell and hold it at a constant uniform temperature. Here, we employed two main design features, (i) the absorption cell was centered inside a vacuum jacket to minimize thermal conductive/convective coupling to the outside cell and (ii) heating/cooling was supplied by temperature-controlled fluid in direct contact with almost the complete cell body. Some of the details are illustrated in Fig. 3, a cross section of the vacuum jacket (1) and the cell (3). When operated above room temperature, heat loss through the insulated support rods (2), is compensated through the use of heaters (4). Welded to the outside of the cell are channels (10) that guide the cooling/heating fluid back and forward along the full length of the cell as shown in Fig. 4. The inlet (6) and outlet (7) are located in adjacent channels to minimize thermal gradients. The standard error (specified by the supplier) for T type thermocouples is ± 1 K. The readings of cell thermocouples were measured with a Standford Research Systems SR630 thermocouple monitor. Heating/cooling was provided by a Neslab ULT-80 thermal bath using Fluorinert electronic fluid FC-77.

To measure the temperature of gas samples, thermocouples are mounted inside the cell. The thermocouple wires pass through the gas outlet and then through four stainless steel tubes, (8) equally spaced by yoke-like mounts (9). The thermocouple tubes have slots where the thermocouple point welds are in direct contact with the gas sample. The locations of the T type thermocouples are shown in Fig. 5.

The gas cell has gas inlet and outlet fittings at opposite ends to allow continuous flow of the gas sample when necessary. The heat carrier channels are terminated before the gas inlet and outlet fittings, i.e. the fittings penetrate the wall of the gas cell. During operation the vacuum jacket was pumped down to pressures as low as 4×10^{-6} Torr.

2.4. Thermal performance of the system

The temperature performance of the cell was tested in two ways. After setting the circulator to a desired temperature, the system was allowed to reach thermal equilibrium (1.5–4 h). On the first test, only the thermocouple readings were compared. Near 225 K the mean temperature of the thermocouples immersed in the gas was 225.61 ± 0.31 K and for those on the surface of the cooling jacket it was 230.05 ± 4.33 K. Near 348 K, the corresponding readings were 348.19 ± 0.17 and 351.75 ± 1.01 K, respectively. Clearly, the surface measurements are less reliable than the gas measurements, showing both a bias to high values and larger deviations and therefore larger temperature gradients.

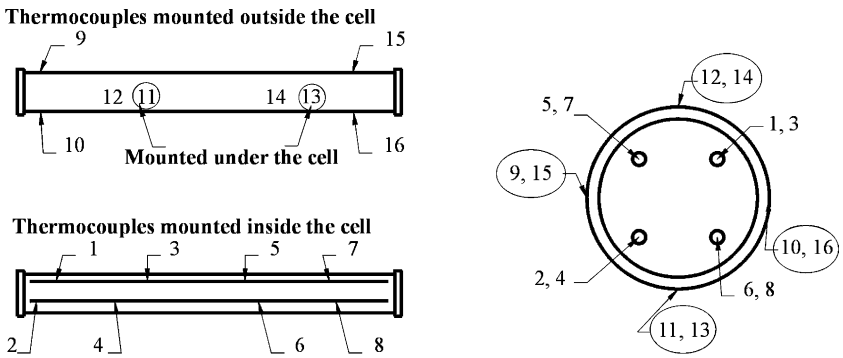

Fig. 5. View of the absorption cell showing the positions of the thermocouples.

The second test was a test of the thermocouples themselves. Here, we measured the line strength, or more precisely the ratios of line strength in the CO second overtone spectrum, and compared these ratios with those calculated using data given in the HITRAN database [11].

The temperature dependence of any spectral line can be determined using the line intensity expression given by

$$S_i = \frac{S_\nu g_i \upsilon_i}{\upsilon_0} \frac{e^{-E_i''/kT}}{Q_{rot}} (1 - e^{-hc\upsilon_i/kT}) L_H |R_{3-0}|^2 \quad (1)$$

In this expression, S_ν is band intensity, g_i, the degeneracy including the weight of nuclear spins, T, the temperature of the gas sample, υ_i the transition wavenumber, υ_0 is the band origin, E_i'' the lower state energy, $Q_{rot}(T)$ the rotational partition function, L_H the Höln–London factor and $|R_{3-0}|^2$ is the reduced matrix element for the band. At any temperature, the internal molecular partition function can be written as $Q(T) = Q_{vib}(T)Q_{rot}(T)$. There are several measurements of S_ν available in the literature [2,6,7]. The transition wavenumbers and lower state energies were taken from the HITRAN molecular database [11]. In the ratio of two line strengths many terms cancel out leaving a temperature-dependent value that depends mostly on the energy level spacings.

Fig. 6 shows measured spectroscopic ratios of the S_{R3} to S_{R11} transition of the $3 \leftarrow 0$ band of CO in the range of 343 to 353 K. The solid line is the value calculated using HITRAN data. The temperature for the experimental points is the mean internal thermocouple reading. Clearly, the internal thermocouples yield a reliable measure of the gas temperature. In fact, the process can be reversed, i.e. the ratios of the two intensities can be used to determine the temperature. This approach was applied to several

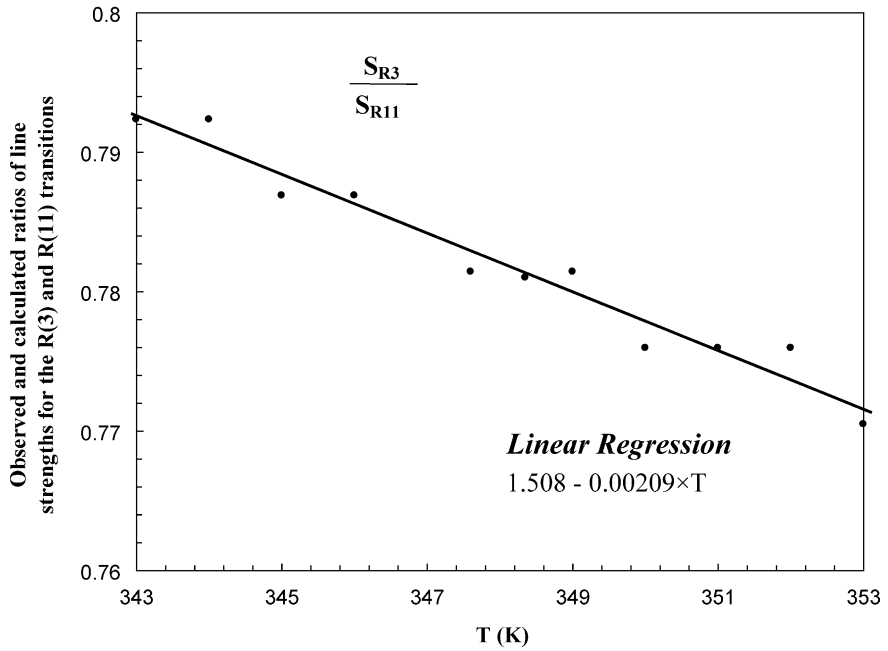

Fig. 6. The ratios of line strengths for the R(3) and R(11) CO transitions as a function of temperature. The solid line is calculated based on the experimental values.

Table 1
Comparison between the rotational gas temperatures and the averaged thermocouple readings for the 147.5-cm cell

Chiller set point (K)	Ratio of S_R for R-branch ransitions	Linear regression curve	Ratio of experimental line strengths	Calculated rotational gas temperature (K)	Averaged readings of the thermocouples mounted inside the cell (K)	Averaged readings of the thermocouples mounted outside the cell (K)	Obs. − calcd temperature (K)
223.25	S_{R3}/S_{R11}	$2.89400 - 0.00705T$	1.3049	225.51 ± 0.21	225.61 ± 0.31	230.05 ± 4.33	0.10
223.25	S_{R4}/S_{R11}	$3.20231 - 0.00756T$	1.5496	225.69 ± 0.21	225.61 ± 0.31	230.05 ± 4.33	−0.08
223.25	S_{R2}/S_{R11}	$1.80726 - 0.00412T$	0.8776	224.64 ± 0.21	225.61 ± 0.31	230.05 ± 4.33	−0.03
223.25	S_{R3}/S_{R10}	$2.21271 - 0.00492T$	1.1016	225.65 ± 0.21	225.61 ± 0.31	230.05 ± 4.33	−0.04
223.25	S_{R4}/S_{R9}	$1.90497 - 0.00355T$	1.1036	225.60 ± 0.21	225.61 ± 0.31	230.05 ± 4.33	0.01
223.25	S_{R3}/S_{R9}	$1.74060 - 0.00345T$	0.9625	225.40 ± 0.21	225.61 ± 0.31	230.05 ± 4.33	0.21
351.15	S_{R4}/S_{R9}	$1.13114 - 0.00127T$	0.8191	348.19 ± 0.10	348.19 ± 0.17	351.75 ± 1.01	0.00
351.15	S_{R3}/S_{R11}	$1.14347 - 0.00154T$	0.6073	348.17 ± 0.10	348.19 ± 0.17	351.75 ± 1.01	0.02
351.15	S_{R3}/S_{R10}	$1.40083 - 0.00194T$	1.0564	348.15 ± 0.10	348.19 ± 0.17	351.75 ± 1.01	0.04
351.15	S_{R3}/S_{R9}	$1.50800 - 0.00209T$	0.7815	348.22 ± 0.10	348.19 ± 0.17	351.75 ± 1.01	−0.03
351.15	S_{R4}/S_{R11}	$1.67134 - 0.00214T$	0.9272	348.35 ± 0.10	348.19 ± 0.17	351.75 ± 1.01	−0.16
351.15	S_{R4}/S_{R9}	$1.23788 - 0.0012T$	0.6903	348.40 ± 0.10	348.19 ± 0.17	351.75 ± 1.01	−0.21

R branch transitions of the $3 \leftarrow 0$ band of CO recorded at 225 K. Consider as an example the case of the R(3) and R(10) transitions. The experimental line strengths were $S_{R3} = 1.9136 \times 10^{-23} \pm 4.8 \times 10^{-26}$ cm^{-1}/molecule cm^{-2} and $S_{R10} = 1.7371 \times 10^{-23} \pm 5.6 \times 10^{-26}$ cm^{-1}/molecule cm^{-2}, leading to an experimental ratio $S_{R3}/S_{R10} = 1.1016$. The calculated linear regression curve based on HITRAN [11] values for S_{R3} and S_{R10} for a range of 10 K around 225 K was $S_{R3}/S_{R10}(T) = 2.21271 - 0.00492T$. The rotational gas temperature was thus found to be $T = 225.65 \pm 0.21$ K, in very good agreement with the averaged readings of the thermocouple mounted inside (225.61 ± 0.31 K) and close to the set point of the chiller of 223.25 K. A comparison of spectroscopic and thermocouple temperatures for two temperatures is given in Table 1, using a selection of line intensity ratios. The measured and calculated temperatures consistently agree to 0.21 K or better. Clearly, the cell performs exceptionally well at providing a well-determined temperature over the length of the cell and over the range of temperatures from 225 to 350 K.

Table 2
Summary of experimental conditions for FTIR CO and CO–N_2 spectra in the $3 \leftarrow 0$ band

Temperature (°C)	Absorber	Broadening gas	CO volume mixing ratio (%)	Optical path (cm)	Pressure (Torr)
25.0	CO	CO	100	25.06	75.25
25.0	CO	CO	100	25.06	350.72
25.0	CO	CO	100	25.06	500.25
25.0	CO	CO	100	25.06	850.13
75.0	CO	CO	100	25.06	200.85
75.0	CO	CO	100	25.06	400.15
75.0	CO	CO	100	25.06	685.19
75.0	CO	CO	100	25.06	970.15
50.0	CO	CO	100	25.06	265.88
50.0	CO	CO	100	25.06	801.55
25.5	CO	N_2	1.0	147.5	690.36
25.5	CO	N_2	1.0	147.5	406.32
25.4	CO	N_2	1.0	147.5	205.62
25.6	CO	CO	100	147.5	5.43
25.6	CO	CO	100	147.5	20.36
75.1	CO	N_2	1.0	147.5	799.85
74.9	CO	N_2	1.0	147.5	599.79
74.6	CO	N_2	1.0	147.5	300.46
50.0	CO	N_2	1.0	147.5	762.87
50.0	CO	N_2	1.0	147.5	501.98

Conversion factors: 1 atm = 760 Torr = 101.3 kPa.

3. High resolution absorption spectra of CO

In the first part of this paper we used the measured spectra to extract the line strength, a property of isolated molecules. In this section, we extend the measurements and extract the width and shift of the lines, properties that reflect the effect of perturbers. As mentioned in Section 1, the widths and shifts and their temperature dependence are essential input parameters for all models of atmospheric absorption.

Ten FTS $CO–N_2$ spectra with $0.015\ cm^{-1}$ resolution were recorded using the 147.5 cm long cell described in Section 2.4 and 10 additional CO spectra were recorded with a short (25-cm-long) heatable cell [14], equipped with CaF_2 windows. The thermal performance of this second cell has been evaluated in the past and compares well with the newly built temperature-variable long cell. The small cell is provided with five thermocouples. The rotational gas temperature agrees within 0.3 K with the thermocouple readings for temperatures ranging from room temperature to 350 K. A summary of the experimental conditions for all spectra used is presented in Table 2. The 1% mixture of $CO–N_2$ was purchased from Matheson Gases. The gas pressure inside the cell was measured with an MKS 120 AA capacitance manometer calibrated by the manufacturer to an absolute accuracy of

Table 3
Lorentz self-broadening and shifting coefficients (cm^{-1} atm^{-1} at 296 K) in the $3 \leftarrow 0$ band of carbon monoxide

m	Broadening coefficients (cm^{-1} atm^{-1} at 296 K)	n	Self-shift coefficients (cm^{-1} atm^{-1} at 296 K)	n'	n'' ($10^{-5}cm^{-1}$ atm^{-1} K^{-1})
−20	0.05341(29)	0.633(35)	−0.00845(50)	1.09(32)	2.73(4)
−19	0.05483(27)	0.632(36)	−0.00817(45)	1.06(31)	2.56(4)
−18	0.05775(28)	0.637(33)	−0.00842(43)	1.08(32)	2.69(3)
−17	0.05804(25)	0.623(29)	−0.00816(41)	1.01(28)	2.44(3)
−16	0.05926(29)	0.625(28)	−0.00776(39)	1.12(22)	2.56(3)
−15	0.06003(26)	0.620(26)	−0.00792(39)	0.96(25)	2.27(2)
−14	0.06102(24)	0.599(30)	−0.00782(39)	1.14(22)	2.62(3)
−13	0.06167(20)	0.576(29)	−0.00779(38)	1.08(18)	2.50(3)
−12	0.06275(18)	0.557(28)	−0.00769(38)	1.13(25)	2.56(3)
−11	0.06313(15)	0.564(27)	−0.00761(38)	1.22(28)	2.72(3)
−10	0.06452(12)	0.570(29)	−0.00757(37)	1.27(30)	2.81(3)
−9	0.06524(11)	0.559(30)	−0.00754(37)	1.17(22)	2.61(3)
−8	0.06632(12)	0.580(27)	−0.00744(37)	1.36(23)	2.94(3)
−7	0.06775(11)	0.577(21)	−0.00728(36)	1.31(21)	2.78(3)
−6	0.06913(11)	0.585(27)	−0.00719(37)	1.27(26)	2.67(3)
−5	0.07124(15)	0.591(28)	−0.00699(36)	1.38(22)	2.81(3)
−4	0.07452(18)	0.619(25)	−0.00651(35)	1.53(30)	2.87(4)
−3	0.07708(17)	0.668(27)	−0.00605(35)	1.59(26)	2.76(4)
−2	0.08116(24)	0.712(30)	−0.00565(34)	1.51(31)	2.44(3)
−1	0.08789(36)	0.734(33)	−0.00512(33)	1.60(35)	2.38(3)
1	0.08742(35)	0.735(32)	−0.00411(32)	0.98(35)	1.21(3)
2	0.08183(26)	0.719(30)	−0.00506(33)	1.08(27)	1.62(3)
3	0.07827(17)	0.671(26)	−0.00577(32)	1.24(26)	2.11(2)
4	0.07462(14)	0.629(25)	−0.00615(34)	1.29(25)	2.33(3)
5	0.07195(13)	0.611(27)	−0.00655(35)	1.48(26)	2.80(4)
6	0.06948(10)	0.584(25)	−0.00681(36)	1.55(25)	3.02(4)
7	0.06749(10)	0.582(23)	−0.00697(37)	1.55(27)	3.10(4)
8	0.06603(11)	0.595(26)	−0.00711(36)	1.51(29)	3.09(4)
9	0.06524(10)	0.570(24)	−0.00716(37)	1.52(30)	3.14(4)
10	0.06427(10)	0.563(26)	−0.00718(38)	1.49(31)	3.09(4)
11	0.06305(13)	0.572(29)	−0.00728(39)	1.39(29)	2.93(4)
12	0.06223(17)	0.575(28)	−0.00738(39)	1.35(27)	2.90(3)
13	0.06162(19)	0.592(27)	−0.00731(38)	1.36(30)	2.88(3)
14	0.06016(23)	0.608(27)	−0.00745(39)	1.25(29)	2.73(3)
15	0.05905(22)	0.620(29)	−0.00748(39)	1.20(29)	2.64(3)
16	0.05822(24)	0.622(32)	−0.00752(45)	1.24(31)	2.73(3)
17	0.05724(23)	0.631(33)	−0.00773(50)	1.06(32)	2.41(3)
18	0.05732(22)	0.637(32)	−0.00802(47)	1.13(32)	2.66(3)
19	0.05533(23)	0.630(35)	−0.00802(48)	1.07(33)	2.54(4)
20	0.05426(24)	0.635(36)	−0.00831(50)	0.95(32)	2.34(4)

The numbers in parentheses are one standard deviation in units of the last digit quoted.

0.05% of the full-scale reading. The pressure inside the vacuum jacket was monitored using a cold cathode gauge (Penning gauge). A quartz-halogen source, a liquid-nitrogen-cooled InSb detector and a CaF_2 beamsplitter inside the FTS were used. All the spectra were recorded at 0.015 cm^{-1} resolution. The estimated uncertainty in the pressure and temperature measurements were 0.1% and 0.3 K (based on retrieved rotational gas temperatures), respectively.

The first step in the analysis was to perform the wavelength calibration of all the spectra. The wavenumber scales of the spectra were calibrated using positions of water vapor lines reported by Toth in his 1998 study of water lines [12]. The water vapor lines used for the calibration were produced by absorption of residual water within the evacuated spectrometer tank. For the majority of the CO lines the absolute uncertainty in our measured line center positions is about ± 0.0001 cm^{-1} or better, as determined by the least-squares procedure. The absolute accuracy of the line positions, however, is dependent upon the accuracy of the water vapor line positions used in calibrating the wavelength scales of the spectra.

The spectral profiles were analyzed using a multi-spectrum fit technique [13] and asymmetric Voigt profiles,

$$I_i(\upsilon) = \frac{S_i}{\pi}\left[\frac{\gamma_i}{(\upsilon-\upsilon_i-\delta_i)^2+\gamma_i^2} + Y_i\frac{(\upsilon-\upsilon_i-\delta_i)}{(\upsilon-\upsilon_i-\delta_i)^2+\gamma_i^2}\right] \quad (2)$$

Table 4
Lorentz nitrogen-broadening and shifting coefficients (cm^{-1} atm^{-1} at 296 K) in the 3 ← 0 band of CO

m	N_2 broadening coefficients (cm^{-1} atm^{-1} at 296 K)	n	N_2 Shift coefficients (cm^{-1} atm^{-1} at 296 K)	n'	n'' (10^{-5} cm^{-1} atm^{-1} K^{-1})
−20	0.05009(34)	0.640(30)	−0.00733(49)	0.86(31)	1.91(4)
−19	0.05135(33)	0.638(38)	−0.00732(49)	0.88(33)	1.93(4)
−18	0.05219(28)	0.647(28)	−0.00737(46)	0.86(31)	1.90(3)
−17	0.05276(27)	0.633(28)	−0.00725(43)	1.06(27)	2.28(3)
−16	0.05390(25)	0.619(25)	−0.00733(42)	0.84(28)	1.90(3)
−15	0.05449(24)	0.623(27)	−0.00719(41)	0.85(28)	1.83(3)
−14	0.05533(22)	0.594(33)	−0.00694(40)	1.01(18)	2.08(3)
−13	0.05634(20)	0.567(28)	−0.00683(39)	0.85(17)	1.73(2)
−12	0.05704(18)	0.543(27)	−0.00659(39)	1.05(20)	2.05(2)
−11	0.05737(17)	0.525(29)	−0.00661(38)	0.88(22)	1.74(2)
−10	0.05822(12)	0.543(28)	−0.00658(36)	0.94(24)	1.85(2)
−9	0.05875(13)	0.551(30)	−0.00652(37)	0.98(21)	1.89(2)
−8	0.05960(12)	0.579(28)	−0.00639(37)	0.92(20)	1.75(2)
−7	0.06068(15)	0.567(20)	−0.00631(38)	1.03(22)	1.92(2)
−6	0.06220(13)	0.565(30)	−0.00608(38)	0.91(24)	1.66(2)
−5	0.06443(16)	0.581(28)	−0.00582(35)	1.15(23)	1.97(2)
−4	0.06691(17)	0.611(25)	−0.00526(36)	0.95(28)	1.50(3)
−3	0.07022(17)	0.688(27)	−0.00506(34)	1.19(31)	1.76(3)
−2	0.07405(29)	0.722(27)	−0.00424(34)	0.94(32)	1.18(3)
−1	0.07897(38)	0.754(31)	−0.00383(32)	1.02(32)	1.14(4)
1	0.07890(36)	0.736(30)	−0.00355(32)	0.71(32)	0.74(4)
2	0.07413(29)	0.709(28)	−0.00422(30)	0.93(27)	1.17(4)
3	0.07046(19)	0.675(27)	−0.00479(31)	0.97(26)	1.38(3)
4	0.06699(18)	0.618(23)	−0.00511(32)	1.04(25)	1.58(3)
5	0.06433(16)	0.601(26)	−0.00562(34)	1.11(26)	1.83(3)
6	0.06214(15)	0.566(22)	−0.00587(35)	1.11(23)	1.92(2)
7	0.06064(14)	0.562(20)	−0.00594(37)	1.10(22)	1.93(2)
8	0.05951(13)	0.590(22)	−0.00603(38)	1.07(24)	1.91(2)
9	0.05867(14)	0.554(24)	−0.00617(38)	1.06(28)	1.93(2)
10	0.05797(12)	0.566(25)	−0.00624(38)	1.12(29)	2.06(3)
11	0.05723(13)	0.566(28)	−0.00614(40)	1.21(28)	2.17(3)
12	0.05651(16)	0.573(26)	−0.00629(40)	1.08(29)	2.01(3)
13	0.05582(18)	0.591(27)	−0.00648(38)	1.18(30)	2.25(3)
14	0.05515(25)	0.610(28)	−0.00655(39)	1.05(31)	2.03(3)
15	0.05444(27)	0.626(29)	−0.00659(44)	1.20(29)	2.32(4)
16	0.05346(26)	0.642(30)	−0.00667(43)	1.31(29)	2.54(4)
17	0.05267(28)	0.639(34)	−0.00698(46)	1.18(31)	2.42(4)
18	0.05167(25)	0.642(35)	−0.00721(47)	1.11(32)	2.27(4)
19	0.05093(27)	0.633(36)	−0.00718(48)	1.44(33)	3.03(4)
20	0.05001(29)	0.645(33)	−0.00712(52)	1.62(33)	3.28(4)

The numbers in parentheses are one standard deviation in units of the last digit quoted.

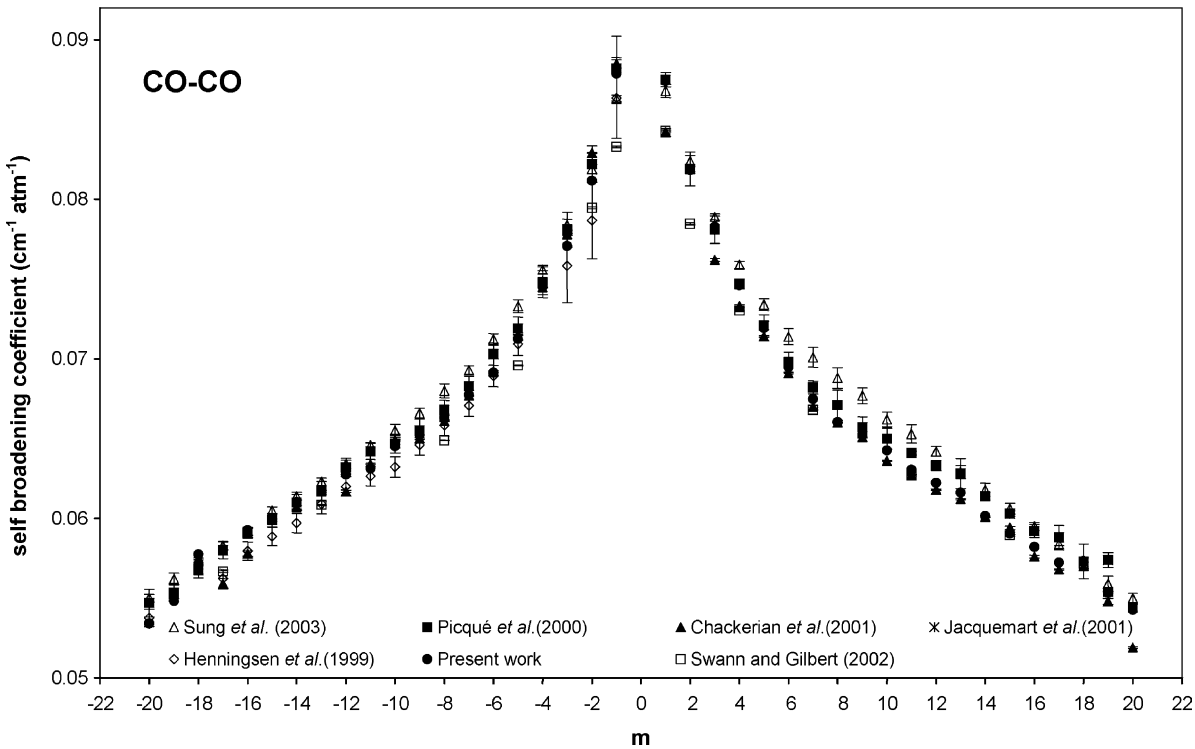

Fig. 7. Lorentz self-broadening coefficients of CO on the 3 ← 0 band as determined from fits of a Voigt profile modified with line mixing in the Rosenkrantz approximation, to the P- and R-branch lines of CO at room temperature.

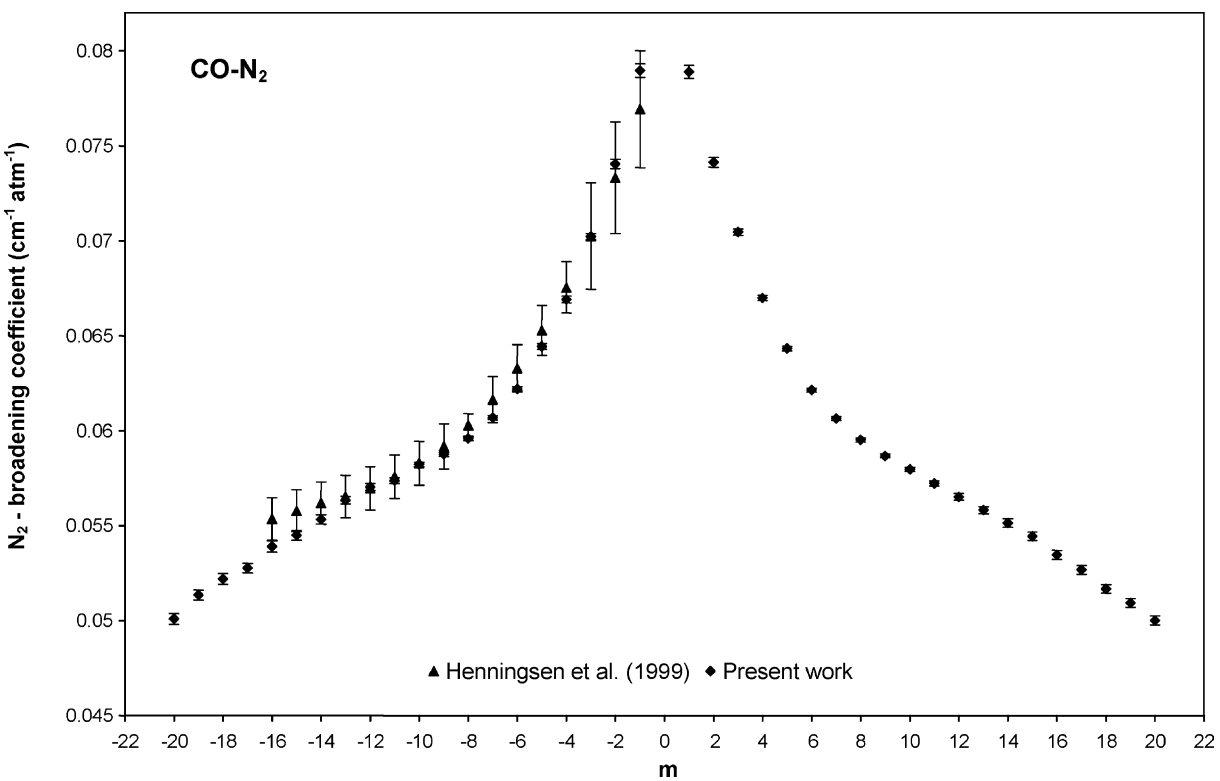

Fig. 8. Lorentz N_2-broadening coefficients of CO on the 3 ← 0 band as determined from fits of a Voigt profile modified with line mixing in the Rosenkrantz approximation, to the P- and R-branch lines of CO at room temperature.

Table 5
Coefficients for power-law polynomials in ln|*m*| for broadening coefficients and their temperature dependence

	Parameter							
	b_0	b_1	b_2	b_3	b_4	b_5	b_6	b_7
Lorentz self-broadening (cm^{-1} atm^{-1} at 296 K)	0.087606	−0.022848	0.049833	−0.066809	0.044441	−0.016511	0.003380	−0.000302
Lorentz N_2broadening (cm^{-1} atm^{-1} at 296 K)	0.078935	0.003538	−0.045848	0.082131	−0.076088	0.036448	−0.008568	0.000781
Temperature dependence of Lorentz self-broadening	0.734527	−0.796243	3.503686	−6.070831	5.125156	−2.283040	0.516283	−0.046682
Temperature dependence of Lorentz N_2-broadening	0.745021	−2.774800	11.035033	−17.251967	13.509253	−5.679264	1.227007	−0.106986

where S_i is the line strength, υ_i the line center position, γ_i the Lorentz half width at half maximum (HWHM), Y_i the line mixing coefficient in the weak mixing limit (Rosenkrantz approximation), and δ_i is the pressure shift.

Measurements of the Lorentz self-broadened widths, N_2-broadened widths, and pressure-induced shifts and their temperature dependence were determined by analyzing *all* spectra simultaneously in spectral segments of 15 cm^{-1} at a time using an interactive multispectral nonlinear least-squares fitting technique. The differences between the experimental spectra and the calculated spectra were minimized by leaving the values of the various line

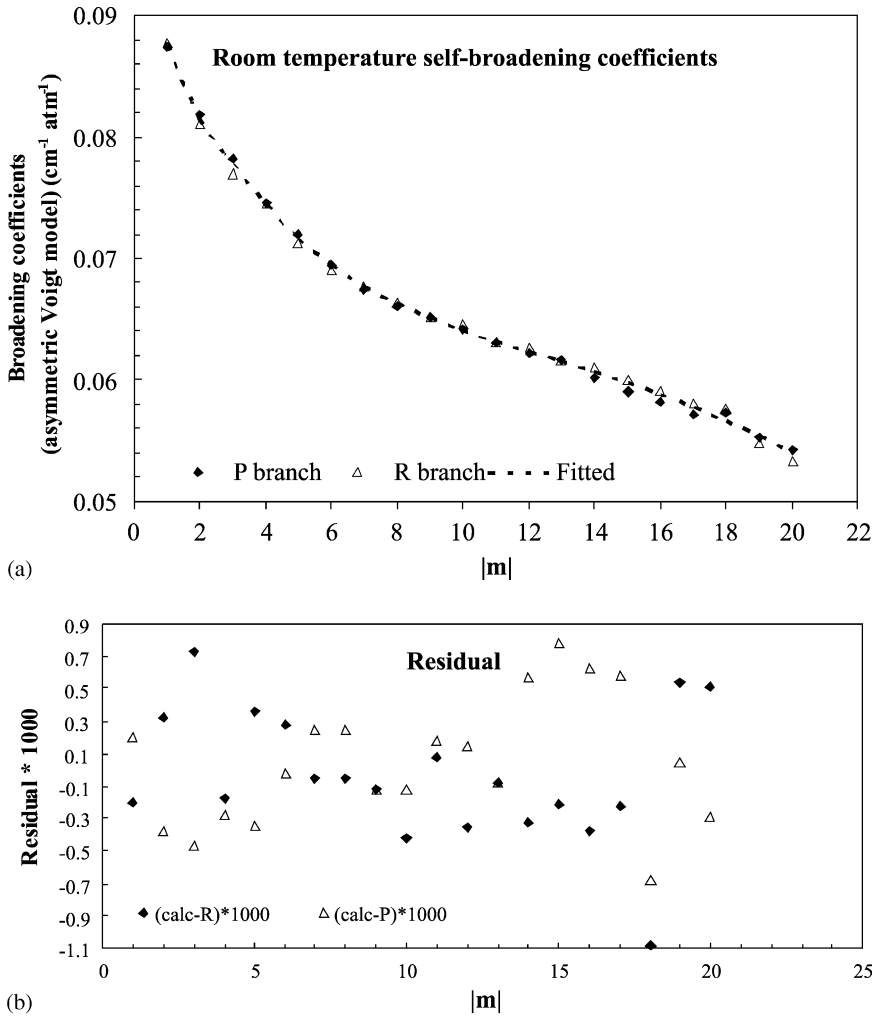

Fig. 9. (a) R- and P-branch Lorentz self-broadening coefficients (Voigt profile modified with line mixing in the Rosenkrantz approximation) as a function of |*m*|. The continuous curve is the polynomial fit to the data. (b) The difference between the experimental R-branch or P-branch data and the polynomial fit to the self-broadening coefficients.

parameters mentioned above as adjustable parameters in the least-squares solution. The absorption features were fitted to a Voigt profile with a line-mixing component in the Rosenkrantz approximation. Initial values for the line positions, intensities, self-broadened widths and pressure-induced shifts were taken from the HITRAN database [11]. The zero percent absorption line for each spectrum was modeled using a fourth order polynomial [13]. The multi-spectrum fits also accounted for the FTS phase error and FTS line shape for the Bomem DA8 instrument. In the analysis, the Doppler-broadened halfwidth of each line was fixed at its theoretical value, calculated as

$$b_D = 3.581 \times 10^{-7} \nu_0 (T/M)^{0.5} \quad (3)$$

where M is the molecular weight of the absorbing gas in atomic mass units, ν_0 the line position in cm^{-1}, T the temperature in K and b_D the Doppler-broadened halfwidth in cm^{-1}/atm.

The expressions used in the global least-squares fitting program for determining the pressure broadening coefficients and pressure-shift coefficients were

$$\nu = \nu_0 + \delta^0 p, \quad \text{and} \quad \Gamma(p,T) = p\gamma(T_0)(T_0/T)^n \quad (4)$$

In the above expressions, ν_0 is the line position (in cm^{-1}) at zero pressure, δ^0 the pressure shift in cm^{-1}/atm, Γ represents the line halfwidth in cm^{-1} at pressure p. The temperature dependence of the halfwidth is n, and $\gamma(T_0)$ the broadening coefficient at the reference temperature T_0 (296 K). The temperature dependence of the pressure shifts and broadening coefficients will be discussed in the following sections.

The temperature scaling law for the Voigt broadening coefficients is convenient as it allows experimentalists to bring their data to a common fixed temperature. It provides a convenient way to interpolate between results for different temperatures, and is a valuable tool for atmospheric modeling.

In Tables 3 and 4 we present our Lorentz self- and N_2-broadening and shifting coefficients. The uncertainties listed in parentheses correspond to one standard deviation of

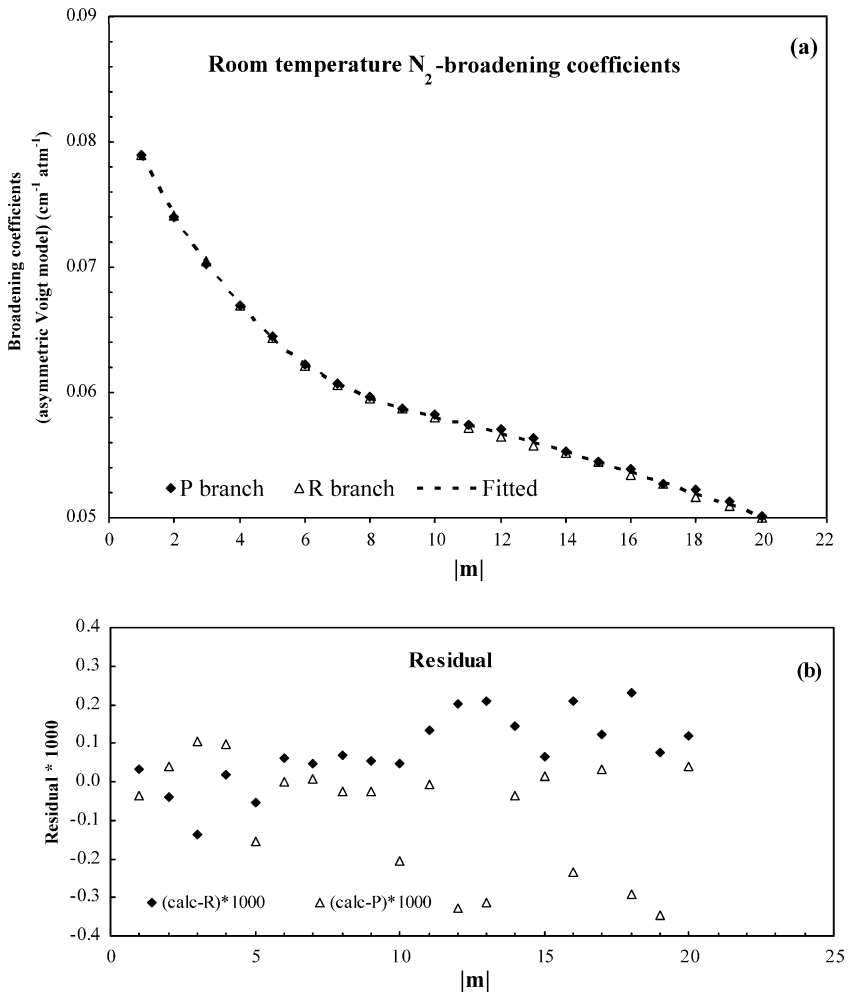

Fig. 10. (a) R- and P-branch Lorentz N_2-broadening coefficients (Voigt profile modified with line mixing in the Rosenkrantz approximation) as a function of $|m|$. The continuous curve is the polynomial fit to the data. (b) The difference between the experimental R- branch or P-branch data and the polynomial fit to the N_2-broadening coefficients.

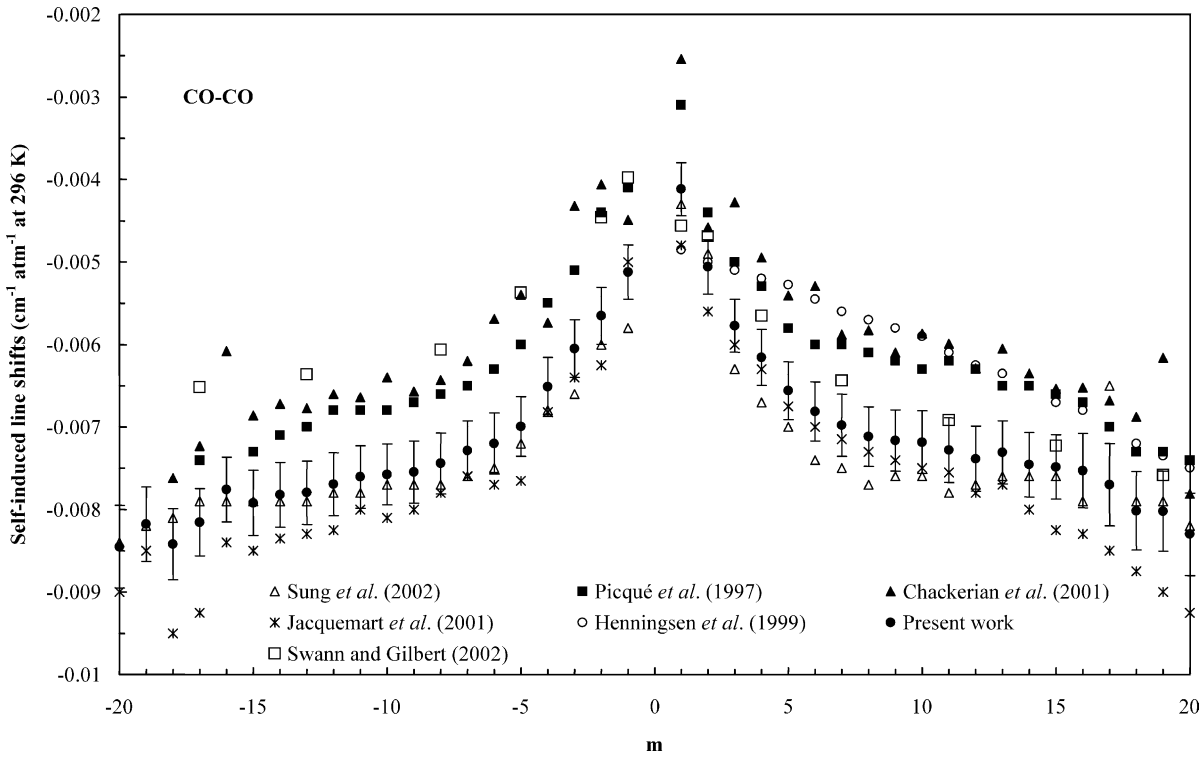

Fig. 11. Self-shifting coefficients as determined from multispectrum fits to the P- and R-branch lines at room temperature.

the measured quantities in units of the last quoted digit. These errors represent only the uncertainties as obtained from the multispectrum least-squares fits and do not reflect errors arising from other systematic sources. Systematic errors arising from sources such as calibration standards, pressure and temperature determinations and uncertainties in the volume mixing ratios of N_2 are difficult to assess, but are probably as large. The accuracy of the line parameters

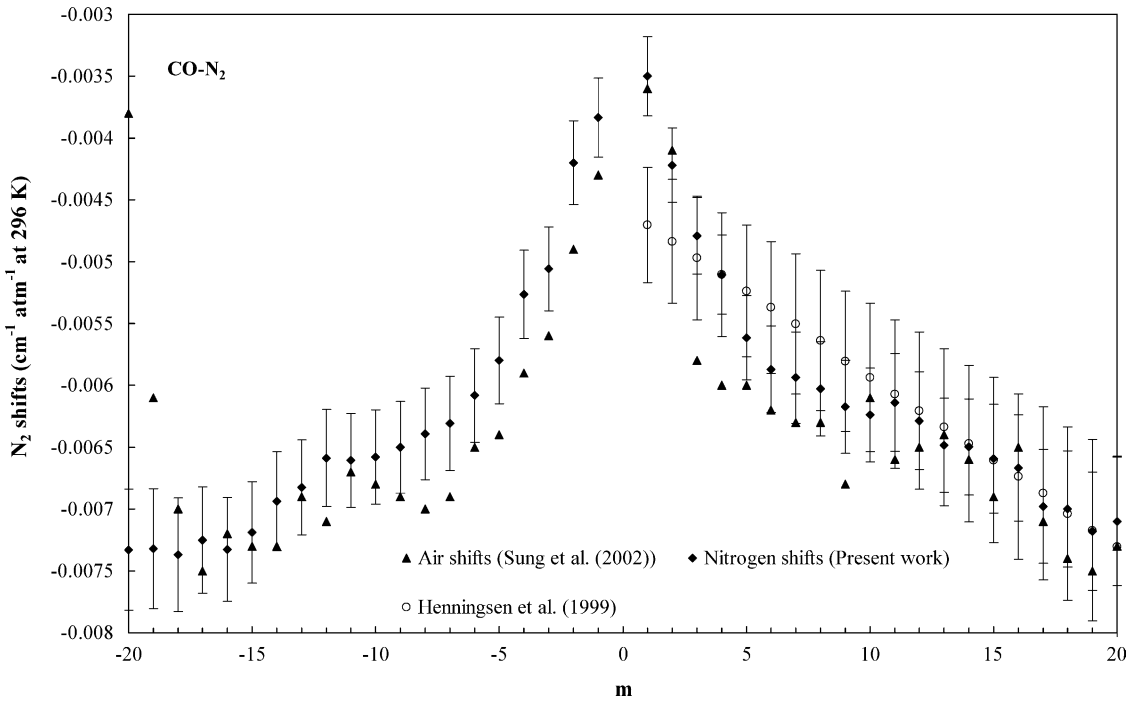

Fig. 12. N_2-shifting coefficients as determined from multispectrum fits to the P- and R-branch lines at room temperature.

listed in Tables 3 and 4 also depends on errors related to the experimental set-up, such as detector nonlinearity, stability of the source, etc. The overall accuracy of the results also depends on the determination of the 100% transmittance level, zero level of the spectrum and background level of the spectra and choice of appropriate line shape model. The multispectrum fitting techniques take into account any zero level offsets by treating them as fitted parameters. Based upon estimated errors due to various sources (calibration of pressure gauges, lack of knowledge of continuum level or zero transmission level, sample purity, phase errors, shape of the instrumental line profile, etc.) the absolute uncertainities in our measured broadening and shifting are 2 and 8% (or better), respectively.

Fig. 7 compares our measurements of the Lorentz self-broadening coefficient with other recent measurements. All results are at room temperature with the width determined by fitting with a Voigt profile modified with line mixing in the Rosenkrantz approximation. Our results agree very well within error bars with measurements from other groups [3,5–9]. Note that for a $P(J)$ transition, m equals $-J$ and for a $R(J)$ transition, m equals $J+1$, where J is the rotational quantum number.

Fig. 8 shows our N_2 broadening results and those of Hennigsen et al. [3], both for room temperature and using a Voigt profile in the fitting routine. The two sets are in agreement within the combined estimated error bars. Our results are more extensive and more precise. To the best of our knowledge there are no theoretical calculations of the broadening coefficients in this band, either for CO–CO or CO–N_2.

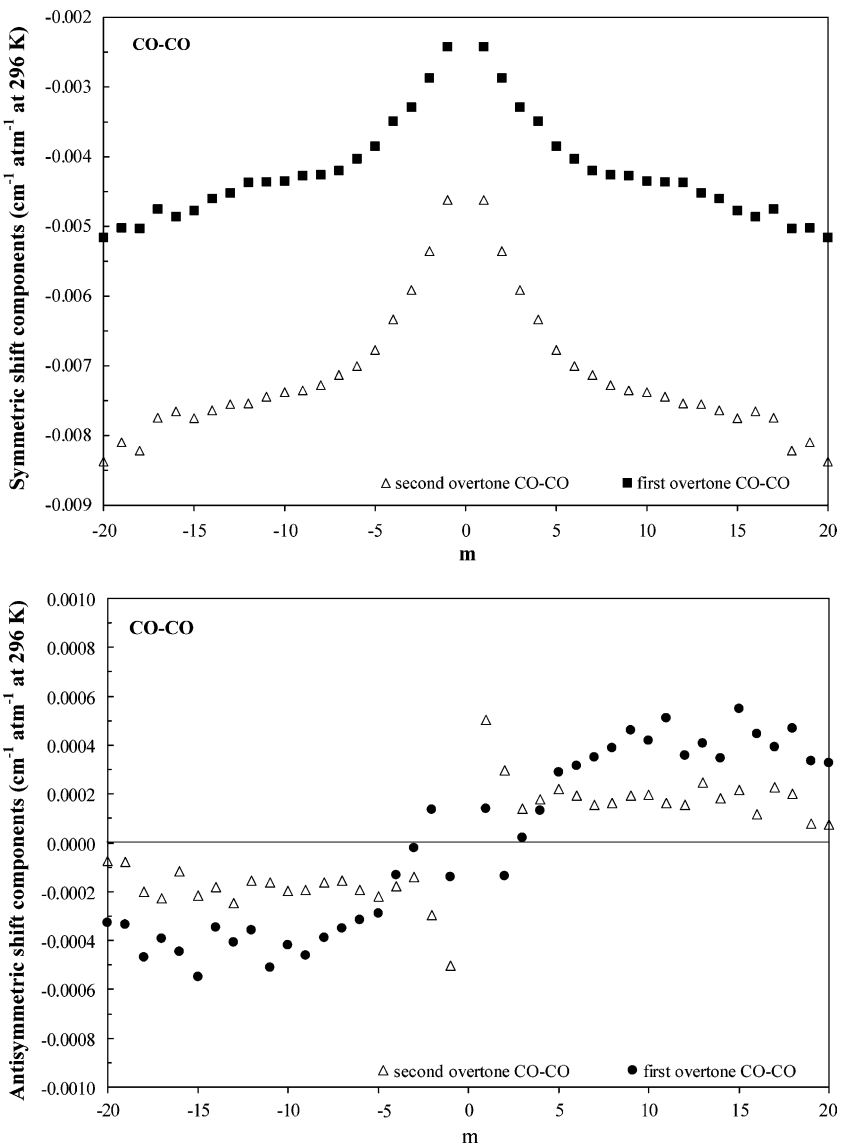

Fig. 13. Symmetric and antisymmetric components of the room temperature line self-shifts in the 3 ← 0 band of CO.

The self- and foreign-broadening coefficients for R branch lines have been fitted to a polynomial:

$$\gamma(m) = b_0 + b_1 \ln|m| + b_2(\ln|m|)^2 + b_3(\ln|m|)^3 + b_4(\ln|m|)^4 + b_5(\ln|m|)^5 + b_6(\ln|m|)^6 + b_7(\ln|m|)^7. \quad (5)$$

The values for the b_0 to b_7 coefficients for self- and N_2-broadened transitions are given in Table 5.

Our values for the broadening coefficient along with the fitted values for the R-branch are shown in Figs. 9a and 10a. Figs. 9b and 10b present the residuals or differences between the experimental R-branch or P-branch data and the polynomial fit to the broadening coefficients. It can be seen that the deviations are small (within the estimated error bars).

The temperature dependence exponents of the broadening coefficients vary with m, indicating a small but noticeable variation of the line shape with rotational quantum number. We have fitted the experimental values for n to the expression:

$$n(m) = b_0 + b_1 \ln|m| + b_2(\ln|m|)^2 + b_3(\ln|m|)^3 + b_4(\ln|m|)^4 + b_5(\ln|m|)^5 + b_6(\ln|m|)^6 + b_7(\ln|m|)^7 \quad (6)$$

Fitted values of the coefficients are given in Table 5.

In addition to the broadening coefficients, we have also retrieved the pressure shifts using the multispectrum fitting technique. The room temperature self- and N_2-pressure shift coefficients obtained in this study are also listed in Tables 3 and 4. The pressure-induced shifts are plotted as a function of m in Figs. 11 and 12 and compared with existing measurements. Our experimental results agree well within error bars with the measurements

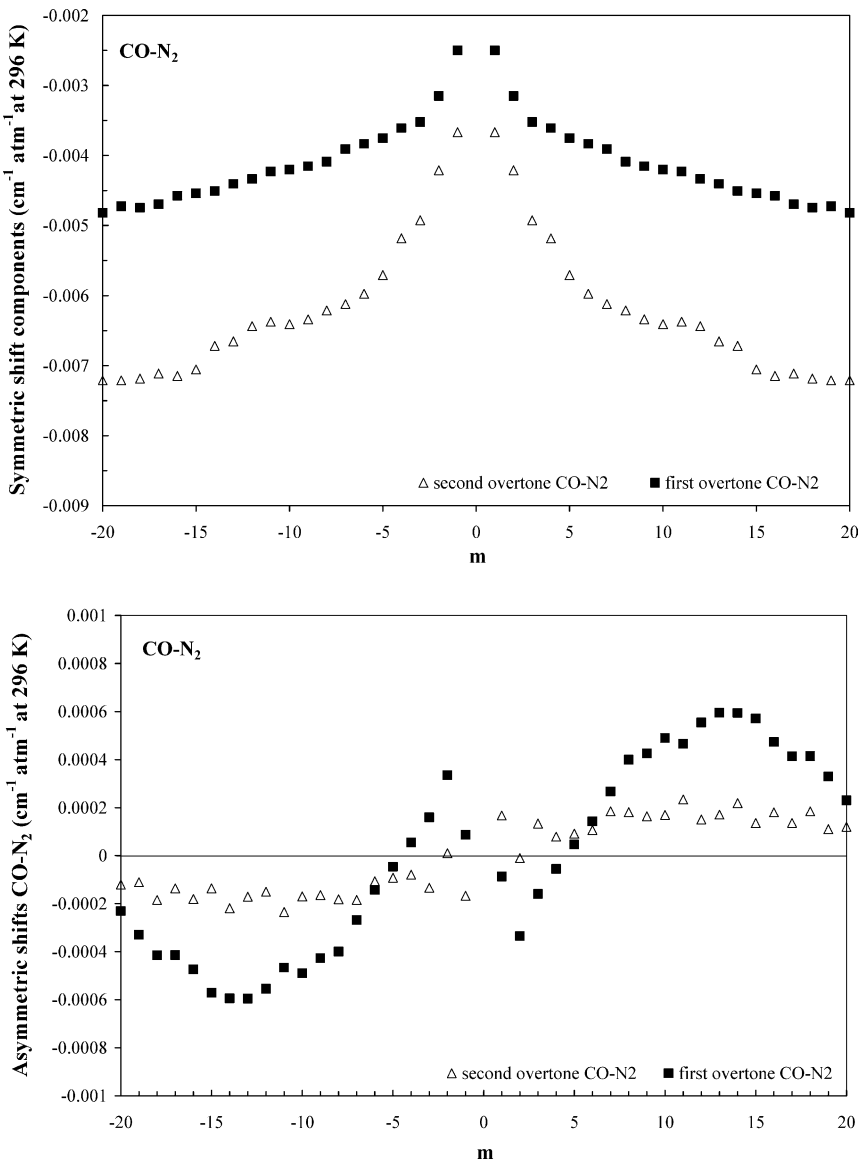

Fig. 14. Symmetric and antisymmetric components of the room temperature line N_2-shifts in the $3 \leftarrow 0$ Band of CO.

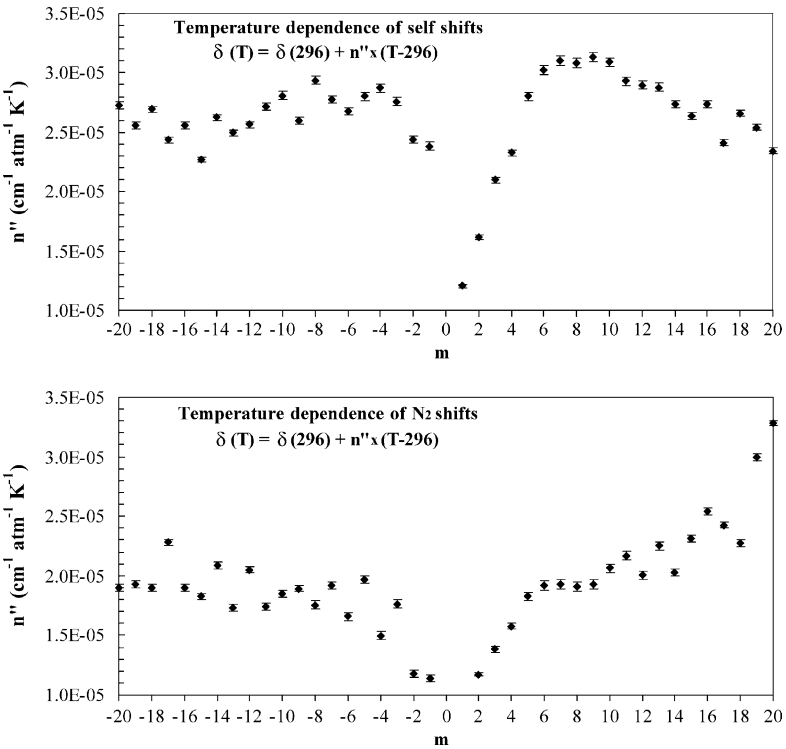

Fig. 15. Temperature dependence coefficient n'' of the line self-shifts and N_2-shifts in the $3 \leftarrow 0$ Band of CO obtained using a temperature scaling law $\delta(T) = \delta(296\ \mathrm{K}) + n''(T - 296\ \mathrm{K})$.

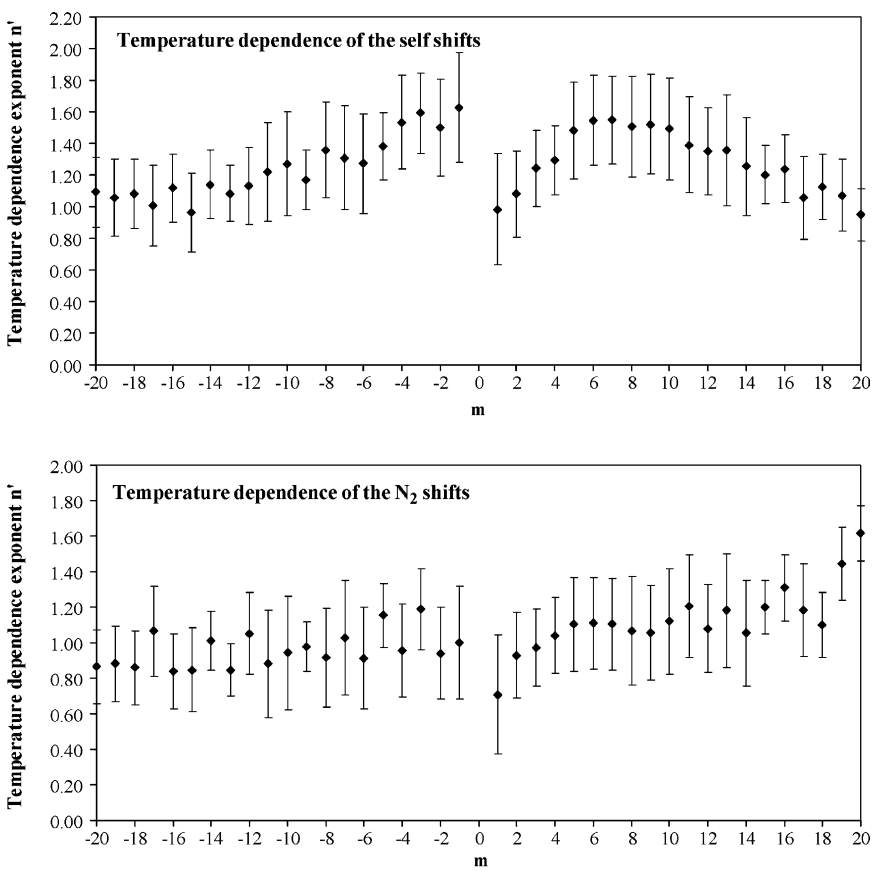

Fig. 16. Temperature dependence coefficient n' of the line self-shifts and N_2-shifts in the $3 \leftarrow 0$ Band of CO obtained using a temperature scaling law $\delta(T) = \delta(296\ \mathrm{K})(T/296\ \mathrm{K})^{-n'}$.

Table 6
Self- and N_2- line mixing coefficients (10^3 atm^{-1} at 296 K) in the $3 \leftarrow 0$ band of carbon monoxide

m	Y_{CO-CO} (10^3 atm^{-1})	Y_{CO-N_2} (10^3 atm^{-1})
−20	3.8(5)	4.7(5)
−19	2.8(3)	2.9(3)
−18	1.1(2)	3.8(4)
−17	2.0(2)	4.1(4)
−16	1.6(2)	3.7(4)
−15	2.8(3)	4.1(3)
−14	1.4(2)	3.1(3)
−13	1.7(3)	2.1(3)
−12	1.4(2)	2.0(2)
−11	1.2(2)	1.4(2)
−10	1.8(2)	2.6(2)
−9	0.8(1)	2.5(2)
−8	1.2(1)	1.2(1)
−7	0.8(1)	0.6(1)
−6	−1.1(1)	0.2(1)
−5	−0.6(1)	−1.6(1)
−4	−1.3(1)	−1.7(2)
−3	−3.8(1)	−3.1(2)
−2	−6.3(1)	−4.8(3)
−1	−6.2(1)	−6.4(5)
0	5.5(1)	5.8(6)
1	4.8(1)	4.4(5)
2	2.3(1)	3.2(4)
3	1.4(1)	1.1(2)
4	0.6(1)	0.6(1)
5	0.2(1)	0.4(1)
6	−1.9(1)	−1.2(1)
7	−2.3(2)	−2.4(2)
8	−3.4(3)	−3.1(3)
9	−3.1(3)	−3.8(3)
10	−4.2(4)	−3.7(3)
11	−3.7(5)	−4.5(4)
12	−4.0(4)	−4.7(4)
13	−4.9(3)	−5.8(5)
14	−6.4(5)	−6.5(5)
15	−6.9(4)	−5.9(5)
16	−6.2(4)	−7.2(5)
17	−5.9(5)	−7.8(6)
18	−7.3(5)	−8.0(5)
19	−8.1(7)	−7.9(6)
20	−7.8(8)	−9.0(7)

The numbers in parentheses are one standard deviation in units of the last digit quoted.

of other authors. It is well known that the pressure shift coefficients are transition dependent. From Figs. 11 and 12, it is clear that unlike the broadening coefficients, the shift coefficients in the two branches show different m dependences.

As shown in Ref. [15] the shifts δ_0 may be decomposed as a function of m into a symmetric component $\delta_{0\text{-}s}$ and an antisymmetric component $\delta_{0\text{-}a}$. Indeed, the vibrational dephasing contribution δ^{iso} coming from the isotropic part of the potential is symmetric in the P-branch with respect to the R-branch, such as $\delta^{iso}(-m) = -\delta^{aniso}(m)$. The symmetric and asymmetric parts of the pressure-induced shift coefficients for $CO-N_2$ and $CO-CO$ are plotted in Figs. 13 and 14. As for broadening, there are no known theoretical calculations of the shifts for this band.

The shift coefficients determined in the present work appear to vary linearly with temperature. We have used a linear expression to model the temperature dependence of the line-shift coefficients using

$$\delta(T) = \delta(296\ \mathrm{K}) + n''(T - 296\ \mathrm{K}) \quad (7)$$

The values obtained for n'' are included in Tables 3 and 4 and are plotted against m in Fig. 15. The limited range of temperatures covered by our spectra affects their overall reliability as far as extrapolation for temperatures outside the 296–348 K range.

A different scaling law for the pressure shifts used by Varanasi's group [15]

$$\delta(T) = \delta(296\ \mathrm{K})(T/296\ \mathrm{K})^{-n'} \quad (8)$$

has also been explored. The results are plotted in Fig. 16 as a function of m. The values obtained for n' show no correspondence in size with the ones for the broadening coefficients (n).

Our analysis using a Voigt profile modified with line mixing in the Rosenkrantz approximation also allowed us to investigate the asymmetric component of the profiles and retrieve the estimated room-temperature line mixing coefficients for CO and $CO-N_2$. In our approach we have neglected the temperature dependence of the line mixing coefficients. The retrieved coefficients are listed in Table 6. The uncertainities given in parentheses represent one standard deviation in the measured quantity as determined by least squares spectrum fits in units of the last digit quoted. In Fig. 17, we plot our room temperature results for CO and $CO-N_2$. The observed antisymmetry with rotational quantum number is consistent with measurements of line mixing coefficients in the $1 \leftarrow 0$ [16] and $2 \leftarrow 0$ bands [14,17]. The mixing coefficients in the R- or P-branches pass through zero near the center of gravity of the branch.

4. Conclusions

In the first part of this paper we have described a new single-path temperature-controlled gas absorption cell design which allows measurements of the spectroscopic parameters of gases over a wide temperature range. Tests of the optical, thermal, and vacuum performance of the facility have been conducted and have successfully demonstrated the capabilities of the facility for use in spectroscopic studies of gases. Particular attention was given to the thermal characteristics of the cell and we demonstrated that the rotational gas temperatures are within ±0.21 K of the averaged readings of

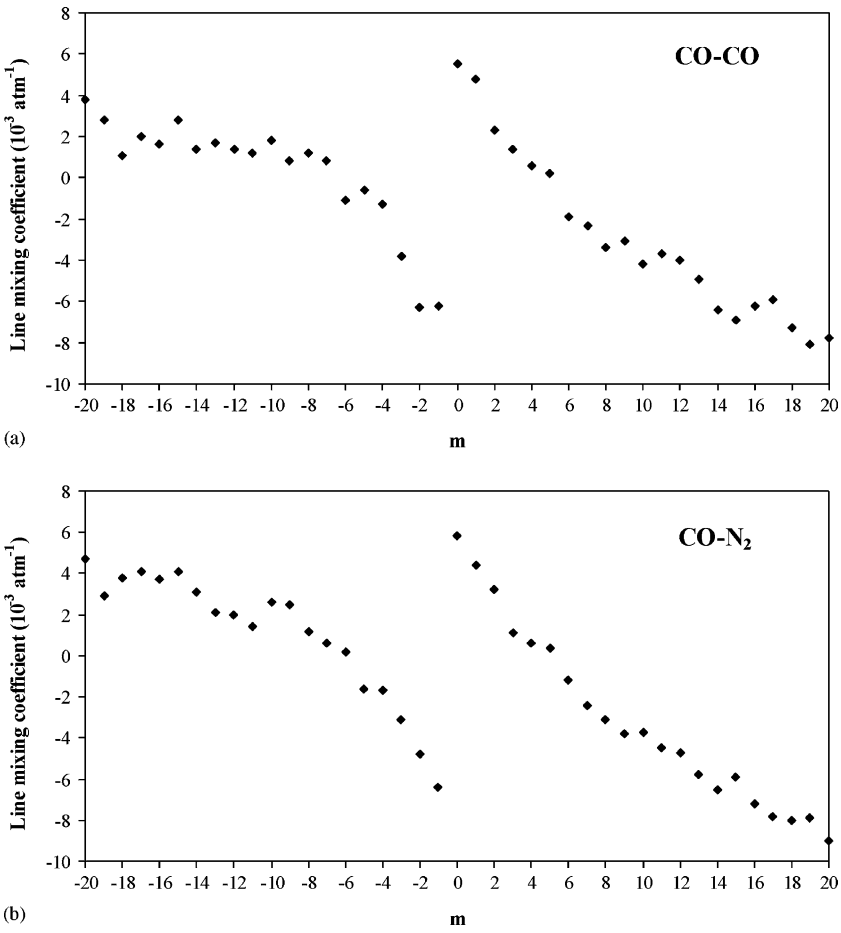

Fig. 17. Line-mixing coefficients for CO and CO–N_2 for P- and R-lines at room temperature.

the thermocouples mounted inside the cell. The temperature gradients inside the cell are within ±0.31 K, highlighting the very good performance of this system.

We have recorded and analyzed the spectral profiles of 20 P and R-branch lines of CO in the 3 ← 0 band broadened by N_2 and self-broadened at temperatures between 225 and 348 K. Our analysis using a Voigt profile modified with line mixing in the Rosenkrantz approximation allowed us to determine the room temperature Lorentz broadening coefficients. The Lorentz broadening coefficients at room temperature are in good agreement with the experimental results of other groups [3,5–9]. The multispectrum fits allowed us to determine the temperature exponent, n, of the Lorentz broadening coefficients. The size of the n coefficients are slightly different for self- and N_2-broadened transitions.

Using our experimental set-up we obtained consistent and accurate results for the pressure-induced shifts in the 3 ← 0 band. Our results are in qualitative agreement with measurements from other groups [2,3,6–9]. There are no theoretical calculations for pressure-induced shifts in this band. We have also examined the temperature dependence of the shifts and based on our limited data set and temperature range coverage, it appears that the shifts follow a linear scaling law with temperature. Lastly, we have retrieved the weak line mixing coefficients. Their size and pattern with m are similar with observations for the lower vibrational bands [14,16,17].

Acknowledgements

The construction of the 147.5 cm cell was supported by funding from the Natural Sciences and Engineering Research Council of Canada. C.H. was supported by the Atmospheric Environment Service and the University of Toronto. A.P.-C. and the Fourier transform spectrometer were supported by the Industrial Research Chair in Atmospheric Remote Sounding from Space. We would also like to thank Mr Gurmit Besla, Mr Alvin Ffrench, Paul Chen and Mr George Bailak for their help and expertise in designing and manufacturing the gas absorption cell. We are thankful to Dr A. David May for helpful comments on the manuscript.

References

[1] J.J. Bel Bruno, J. Gelfand, W. Radigan, K. Verges, Mol. Spectrosc. 94 (1982) 336–342. J.J. Bel Bruno, J. Mol. Spectrosc. 99 (1983) 243–243. Correction.

[2] N. Picqué, G. Guelachvili, J. Mol. Spectrosc. 185 (1997) 244–248.

[3] J. Henningsen, H. Simonsen, T. Mogelberg, E. Trudso, J. Mol. Spectrosc. 193 (1999) 354–362.

[4] C. Hnatovsky, A. Predoi-Cross, K. Strong, J.R. Drummond, D.C. Benner DC, Paper FEW 9 presented at the Topical Meeting entitled '*FTS*—New Applications and Methods' of the Optical Society of America, Santa Barbara, 1999.

[5] N. Picqué, G. Guelachvili,V, V. Dana, J.-Y Mandin, J. Mol. Struct. 517–518 (2000) 427–434.

[6] C. Chackerian Jr., R. Freedman, L.P. Giver, L.R. Brown, J. Mol. Spectrosc. 210 (2001) 119–126.

[7] D. Jacquemart, J.-Y. Mandin, V. Dana, N. Picqué, G. Guelachvili, Eur. Phys. J. D14 (2001) 55–69.

[8] W.C. Swann, S.L. Gilbert, J. Opt. Soc. Am. B 19 (10) (2002) 2461–2467.

[9] K. Sung, P. Varanasi, J. Quantum Spectrosc. Radiat. Transfer 83 (3–4) (2004) 243–265.

[10] Crystran Optics Catalogue, 1999.

[11] L.S. Rothman, A. Barbe, D.C. Benner, L.R. Brown, C. Camy-Peyret, M.R. Carleer, K. Chance, C. Clerbaux, V. Dana, V.M. Devi, A. Fayt, J. Fischer, J.M. Flaud, R.R. Gamache, A. Goldman, D. Jacquemart, K.W. Jucks, W.J. Lafferty, J.Y. Mandin, S.T. Massie, V. Nemtchinov, D.A. Newnham, A. Perrin, C.P. Rinsland, J. Schroeder, K.M. Smith, M.A.H. Smith, K. Tang, R.A. Toth, J. Vander Auwera, P. Varansi, K. Yoshino, The HITRAN molecular spectroscopic database: edition of 2000 including updates through 2001, J. Quantum Spectrosc. Radiat. Transfer 82 (1–4) (2003) 5–44.

[12] R.A. Toth, J. Mol. Spectrosc. 190 (1998) 376–396.

[13] D.C. Benner, C.P. Rinsland, V. Malathy Devi, M.A.H. Smith, D. Atkins, J. Quantum Spectrosc. Radiat. Transfer 53 (6) (1995) 705–721.

[14] A. Predoi-Cross, J.P. Bouanich, D. Chris Benner, A.D. May, J.R. Drummond, J. Chem. Phys. 113 (2000) 158–168.

[15] P. Varanasi, S. Chudamani, J. Quantum Spectrosc. Radiat. Transfer 43 (1990) 1–11.

[16] A. Predoi-Cross, C. Luo, P.M. Sinclair, A.D. May, J.R. Drummond, J. Mol. Spectrosc. 198 (1999) 291–303.

[17] J.W. Brault, L.R. Brown, C. Chackerian Jr., R. Freedman, A. Predoi-Cross, A.S. Pine, J. Mol. Spectrosc. 222 (2) (2003) 220–239.